HHS Public Access

Author manuscript

ACS Appl Mater Interfaces. Author manuscript; available in PMC 2018 July 13.

Published in final edited form as:

ACS Appl Mater Interfaces. 2018 June 13; 10(23): 20055–20063. doi:10.1021/acsami.8b05066.

Bioinspired Photocatalytic Shark-Skin Surfaces with Antibacterial and Antifouling Activity via Nanoimprint Lithography

Feyza Dundar Arisoy[†], **Kristopher W. Kolewe**[‡], **Benjamin Homyak**[†], **Irene S. Kurtz**[‡], **Jessica D. Schiffman**[‡], and **James J. Watkins**[*,†]

[†]Department of Polymer Science and Engineering, University of Massachusetts Amherst, Amherst, Massachusetts 01003, United States

[‡]Department of Chemical Engineering, University of Massachusetts Amherst, Amherst, Massachusetts 01003, United States

Abstract

By combining antifouling shark-skin patterns with antibacterial titanium dioxide (TiO_2) nanoparticles (NPs), we present a simple route toward producing durable multifunctional surfaces that decrease microbial attachment and inactivate attached microorganisms. Norland Optical Adhesive, a UV-crosslinkable adhesive material, was loaded with 0, 10, or 50 wt % TiO_2 NPs from which shark-skin microstructures were imprinted using solvent-assisted soft nanoimprint lithography on a poly(ethylene terephthalate) (PET) substrate. To obtain coatings with an exceptional durability and an even higher concentration of TiO_2 NPs, a solution containing 90 wt % TiO_2 NPs and 10 wt % tetraethyl orthosilicate was prepared. These ceramic shark-skin-patterned surfaces were fabricated on a PET substrate and were quickly cured, requiring only 10 s of near infrared (NIR) irradiation. The water contact angle and the mechanical, antibacterial, and antifouling characteristics of the shark-skin-patterned surfaces were investigated as a function of TiO_2 composition. Introducing TiO_2 NPs increased the contact angle hysteresis from 30 to 100° on shark-skin surfaces. The hardness and modulus of the films were dramatically increased from 0.28 and 4.8 to 0.49 and 16 GPa, respectively, by creating ceramic shark-skin surfaces with 90 wt % TiO_2 NPs. The photocatalytic shark-skin-patterned surfaces reduced the attachment of *Escherichia coli* by ~70% compared with smooth films with the same chemical composition. By incorporating as low as 10 wt % TiO_2 NPs into the chemical matrix, over 95% *E. coli* and up to 80% *Staphylococcus aureus* were inactivated within 1 h UV light exposure because of the photocatalytic properties of TiO_2. The photocatalytic shark-skin-patterned surfaces presented here

[*]Corresponding Author: watkins@polysci.umass.edu.

ORCID

Feyza Dundar Arisoy: 0000-0002-3702-217X Jessica D. Schiffman: 0000-0002-1265-5392

Notes

The authors declare no competing financial interest.

Supporting Information

The Supporting Information is available free of charge on the ACS Publications website at DOI: 10.1021/acsami.8b05066. Profilometry scans of master molds; TGA data of NOA, TiO_2-10, TiO_2-50, and TiO_2–C; TEM micrographs of TiO_2 NPs, TiO_2-10, TiO_2-50, and TiO_2–C films; digital pictures of the shark-skin patterns; SEM micrographs of NOA*; antifouling activity of NOA*; and fluorescent micrographs of *E. coli* adhered to the patterned surfaces (PDF)

were fabricated using a solution-processable and roll-to-roll compatible technique, enabling the production of large-area high-performance coatings that repel and inactivate bacteria.

Graphical Abstract

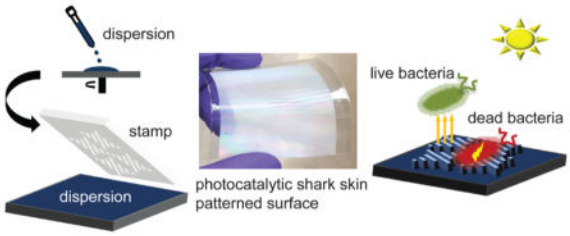

Keywords

antibacterial; antifouling; bioinspired; nanoimprint lithography (NIL); photocatalysis; titanium dioxide

1. INTRODUCTION

Pathogenic microorganisms are transferred to at-risk patients through direct patient or clinician contact with contaminated high-touch surfaces,[1,2] resulting in healthcare-associated infections.[3] Although commercial antibiotics are the most common way to kill bacteria, their misuse and overuse have led to widespread antibiotic resistance, which results in greater than 2 million infections and 23 000 deaths in the United States, per year.[4–6] New coatings for high-touch surfaces, such as bed rails, door knobs, etc., that both limit the attachment of microorganisms and inactivate the persistent microbes are in high demand.[7,8]

Drawing inspiration from nature,[9–12] many biomimetic surface topographies have been shown to reduce microbial adhesion through a biocide-free structure–property relationship.[13–15] For example, the diamondlike riblets on the skin of sharks reduce drag and facilitate self-cleaning.[16–18] Brennan et al. fabricated Sharklet AF, synthetic microstructures in silicone, by replicating a silicon wafer mold prepared using photolithography.[19] Because of their unique hierarchical design and engineered roughness index,[20] Sharklet AF-patterned surfaces effectively inhibited the adhesion of the zoospores, *Ulva* (~5 μm diameter), and *Staphylococcus aureus* (1 μm diameter).[19–22] Furthermore, Reddy et al. reported that silicone Sharklet AF surfaces reduced surface coverage by Gram-negative bacteria *Escherichia coli* by up to 55% and the colony size by 76% compared with smooth films, after a 24 h incubation period.[23] However, Sharklet AF-patterned surfaces share a limitation intrinsic to all microtopographic patterned surfaces: given a sufficient amount of time, bacteria will accumulate on the surface. For this reason, microtopography alone is insufficient and there is a need to develop multifunctional coatings that are antifouling and antibacterial.

Photocatalytic materials, including titanium dioxide (TiO_2), are effective antimicrobial agents that inactivate a wide array of microorganisms including both Gram-positive and -negative bacteria, fungi, and viruses.[24,25] TiO_2-based nanocomposites have been extensively

studied for a variety of applications, including surface disinfectants.[26–28] When TiO_2 absorbs UV light, redox reactions with H_2O or OH^- molecules form reactive hydroxyl radicals and superoxide ions, respectively.[29,30] Interaction of these reactive species with the outer membrane of bacteria induces rupture and subsequent cell death.[25] The benefits of using TiO_2 nanoparticles (NPs) compared to other well-known antibacterial agents (silver, copper, etc.) are their low cost, wide availability, and ability to be incorporated into transparent coatings. These advantages make TiO_2 an attractive candidate for use in high-touch antimicrobial surface coatings.

In this work, we developed multifunctional surfaces by synergistically combining the antibacterial activity of TiO_2 with adhesion-resistant biomimetic shark-skin microtopography. To the best of our knowledge, this work represents the first reported use of antibacterial NPs in shark-skin-patterned surfaces. Orthogonal shark-skin surfaces were fabricated using solvent-assisted nanoimprint lithography (NIL)[31,32] on flexible poly(ethylene terephthalate) (PET) substrates from polymer and ceramic composite dispersions. Polymeric shark-skin composites containing 10 and 50 wt % TiO_2 NPs were prepared using Norland Optical Adhesive (NOA). Ceramic shark-skin was prepared with 90 wt % TiO_2 NPs using tetraethyl orthosilicate (TEOS) as a binder. We further investigated the wettability, mechanical, antibacterial, and antifouling characteristics of the composites and shark-skin-patterned surfaces as a function of TiO_2 composition. Scalable and low-cost photocatalytic shark-skin-patterned surfaces offer high antimicrobial performance toward the development of light-assisted, environmentally friendly antifouling and antibacterial surface coatings.

2. EXPERIMENTAL SECTION

2.1. Materials

All materials were used as received without further purification. Titanium dioxide (TiO_2, anatase phase) nanoparticles (5–30 nm diameter), 15 wt %, dispersed in water were purchased from Nanostructured & Amorphous Materials Inc. (Houston, TX). Norland Optical Adhesive 60 (NOA) was purchased from Norland Products, Inc. (Cranbury, NJ). *N*-Methyl-2-pyrrolidone (NMP, ReagentPlus 99%), M9 minimal salts (M9 media), phosphate-buffered saline (PBS, 10× sterile biograde), and 98% tetraethyl orthosilicate (TEOS) were purchased from Sigma-Aldrich (St. Louis, MO). Poly(vinyl alcohol) (PVOH, 80% hydrolyzed, 6 kg/mol) was purchased from Polysciences, Inc. (Warrington, PA). Methanol (MeOH) and poly(tetrafluoroethylene) (PTFE) filters (0.45 μm) were purchased from Fisher Scientific (Hampton, NH). Poly(ethylene terephthalate) (PET) roll (ST 505, 125 μm thick films), Dupont, was purchased from Tekra Corporation (New Berlin, WI). (Heptadeca-fluoro-1,1,2,2-tetrahydrodecyl)dimethylchlorosilane was acquired from Gelest (Morrisville, PA). The Sylgard 184 silicone elastomer kit (poly(dimethylsiloxane) (PDMS)) was purchased from Dow Corning (Midland, MI).

2.2. Methods

2.2.1. Solvent Exchange of TiO_2 Nanoparticle (NP) Dispersion—The details of solvent exchange can be found in previous publications from our group.[31] Briefly, TiO_2 (100

g of 15 wt %) aqueous dispersion was added into a 250 mL bottle. NMP (50 g) and MeOH (50 g) were added to the dispersion and mixed. The mixed solution was placed under air flow overnight until the majority of the solvent was removed, resulting in a slurry. The amount of the solvent and solid was calculated, and subsequently, NMP and MeOH were added in a 1:1 weight ratio to the slurry mixture to obtain an approximately 15 wt % TiO_2 dispersion. The dispersion was sonicated (~30 min) until stable TiO_2 NP dispersions were obtained. The final TiO_2 concentration was calculated as 15.2 wt % and remained stable for a year.

2.2.2. PDMS Mold Fabrication—Sample compositions are named NOA (100 wt % NOA), TiO_2-10 (10 wt % TiO_2/90 wt % NOA), TiO_2-50 (50 wt % TiO_2/50 wt % NOA), and TiO_2–C (90 wt % TiO_2/10 wt % TEOS).

To fabricate shark-skin patterns from NOA, TiO_2-10, TiO_2-50, and TiO_2–C with the same dimensions, two different masters (Master 1 and Master 2) were used as further explained in Section 3.

2.2.2.1. Master 1: Soft PDMS replica molds were fabricated using the standard fabrication method.[33] PDMS was prepared by mixing Sylgard 184 at a 1:10 ratio of curing agent to base, then poured onto a Sharklet nickel (Master 1; height: 3 μm, width: 2 μm, pitch: 4 μm) mold (provided by Sharklet Technologies), and placed into an oven to be cross-linked at 70 °C for 3 h. The PDMS was then peeled off from Master 1 to obtain a soft mold of the inverse Sharklet structure. The inverse Sharklet PDMS mold was used to imprint TiO_2-50 and TiO_2–C shark-skin patterns.

2.2.2.2. Master 2: A TiO_2-50-patterned shark-skin sample was used as a master mold (Master 2; height: 1.6 μm, width: 1.3 μm, pitch: 4 μm). TiO_2-50 was placed in an oxygen (O_2) plasma cleaner for 2 min, and then the surface was modified with (heptadecafluoro-1,1,2,2-tetrahydrodecyl)-dimethylchlorosilane at 60 °C for 12 h to obtain an antisticking surface. The inverse-shark-skin PDMS mold was prepared from Master 2 using the same procedure given above. The inverse-shark-skin PDMS mold was used to imprint NOA and TiO_2-10 shark-skin patterns.

2.2.3. Shark-Skin Pattern Fabrication Using Solvent-Assisted NIL—PET substrates were cleaned using ethanol and isopropanol, then exposed to O_2 plasma for 3 min, and used as a substrate for the imprints. TiO_2 composite dispersions were prepared using solvent-exchanged 15.2 wt % TiO_2 (NMP/MeOH). To prepare NOA shark-skin patterns, a 20 wt % NOA solution in NMP was spin-coated onto a PET substrate, then a PDMS stamp (replica from Master 2) was placed on top. A TiO_2-10 (10 wt % TiO_2/90 wt % NOA) dispersion was prepared as a 17 wt % (solids) dispersion in NMP/MeOH and spin-coated to form an 800 nm film. A PDMS mold (replica from Master 2) was then placed on top. A TiO_2-50 (50 wt % TiO_2/50 wt % NOA) dispersion was prepared as 30 wt % (solids) dispersion in NMP/MeOH and spin-coated to form an 800 nm film. A PDMS mold (replica from Master 1) was then placed on top. A TiO_2–C (90 wt % TiO_2/10 wt % TEOS) dispersion was prepared as 17 wt % solid in NMP/MeOH and spin-coated to form an 800 nm film. A PDMS mold (replica from Master 1) was then placed on top. The assemblies

were placed on a 50 °C hot plate for 30 min to evaporate residual solvents. NOA, TiO_2-10, and TiO_2-50 assemblies were UV-cured to obtain cross-linked structures (UV light wavelength: 365 nm, with an energy of 11 J/cm^2).[31] A TiO_2–C assembly was near infrared (NIR) (Adphos, 3 kW) irradiated (10 s) to quickly obtain silica binding. For each case, PDMS was gently peeled off from the coating and the shark-skin patterns were obtained. NOA, TiO_2-10, TiO_2-50, and TiO_2–C dispersions were used to fabricate smooth films with the same chemistry as that of the patterned samples. UV- or NIR-curing procedures were conducted for corresponding samples.

2.3. Characterization and Evaluation of Shark-Skin Surfaces

2.3.1. Material Characterization—To prepare thin films for transmission electron microscopy (TEM) imaging, glass substrates were coated with a PVOH sacrificial layer and placed on a hot plate for 1 min. Thin films (~100 nm) of TiO_2-10, TiO_2-50, and TiO_2–C composites were spin-coated onto PVOH. Films were floated on water after PVOH was dissolved and picked up by carbon-coated copper grids for TEM. In addition to composite films, solvent-exchanged TiO_2 NPs in NMP/MeOH were diluted further with NMP/MeOH and drop-casted on a carbon-coated copper grid for TEM characterization. TEM was performed in bright-field imaging mode using a JEOL 2000 FX TEM operated at an accelerating voltage of 200 kV. To measure the mechanical properties of NOA, TiO_2-10, TiO_2-50, and TiO_2–C films, dispersions of each polymer and ceramic composite were spin-coated into films of 800–1200 nm on PET substrates. The hardness and reduced modulus of films were determined using a Hysitron TriboIndenter (TI 950) by averaging 30 indentations obtained under rate control (10 μN/s) using a Berkovich tip (100 nm) for each film. A significant difference was determined by analysis of variance (ANOVA) with the Tukey test. Values of $p < 0.05$ were considered to be significant. The concentration of TiO_2 NPs was confirmed by thermogravimetric analysis (TGA, TA Instruments Q50) using the following temperature program under air: heating from room temperature to 700 °C, with a rate of 10 °C/min. Scanning electron microscopy (SEM) was performed on a field emission SEM (Magellan 400). The NOA and TiO_2-10 shark-skin samples were gold-sputtered using a sputter coater (CR 108) for 45 s prior to imaging. The TiO_2-50 and TiO_2–C shark-skin samples were imaged as-produced in the SEM. A three-dimensional optical profilometer (Zygo, Nexview) was used to measure feature dimensions. Contact angle measurements were acquired using a VCA Optima surface analysis/goniometry system. Prior to testing, shark-skin-patterned samples were kept in the dark for 14 days to minimize UV effects. Static, advancing, and receding water contact angles were determined from parallel and orthogonal directions using six independent measurements at room temperature (5 μL water drops were used).

2.3.2. Antifouling Performance—The fouling resistance of shark-skin-patterned NOA, TiO_2-10, TiO_2-50, and TiO_2–C composites, as well as smooth chemistry controls, was evaluated with a bacterial attachment assay using the model bacteria, *E. coli* K12 MG1655 (*E. coli*, expressing green fluorescent protein).[34] *E. coli* was cultured overnight in Luria-Bertani broth (Sigma-Aldrich) and then washed and re-suspended in M9 media to a final concentration of 1×10^8 cells/ mL. Samples were placed at the base of separate wells in six-well polystyrene plates (Fisher Scientific) and inoculated with 5 mL of *E. coli* suspended in

M9 media. Following a 24 h incubation period at 37 °C, the growth media were removed using a sterilized glass pipette and samples were rinsed repeatedly with PBS before analysis. Samples were analyzed using Zeiss Microscope Axio Imager A2M (20× and 50× magnification, Thornwood, NY). The surface area coverage of attached bacteria was quantified by analyzing 10–15 randomly acquired images over at least three parallel replicates using ImageJ 1.45 software (National Institutes of Health, Bethesda, MD).

2.3.3. Antibacterial Activity—The antibacterial activity of the samples was evaluated using a standard assay modified to expose the samples to UV light.[35] Smooth thin films of TiO_2-10, TiO_2-50, and TiO_2–C were evaluated in parallel with controls including NOA, PET, and glass slides (data not shown). Samples were placed at the base of separate wells in six-well polystyrene plates to which 5 mL of M9 media containing *E. coli* or *S. aureus* SH1000[34] (1×10^8 cells/mL) was added before incubating for 1 h at 37 °C under UV light (F15W/T8 McMaster-Carr, 15 W 365 nm wavelength). Samples were held at a 15 cm fixed distance from the UV source. UV light intensity was measured using a UV light meter (Thorlabs GM10HS, Hamamatsu S2281 probe) and determined to be 1.0 mW/cm^2. Following photoactivation, the samples were removed and stained with propidium iodide (PI) for 15 min to identify the dead cells before being thoroughly washed with PBS to remove excess stain. The loss of viability was visualized using Zeiss Microscope Axio Imager A2M, quantified using ImageJ software, and the percentage of dead cells (or loss of viability) was calculated from the ratio of the number of cells stained with PI divided by the total number of cells.[35]

2.3.4. Statistics—Significant differences between antifouling/ antibacterial samples were determined with an unpaired Student *t*-test. The significance is denoted in the graphs using asterisks and defined in the figure captions.

3. RESULTS AND DISCUSSION

3.1. Polymer and Ceramic Composite Shark-Skin-Pattern Fabrication

Orthogonal shark-skin microstructures were successfully imprinted using TiO_2-loaded dispersions via solvent-assisted NIL,[31,32] as shown in Scheme 1. The Master 1 mold (height: 3 μm, width: 2 μm, pitch: 4 μm) and the Master 2 mold (height: 1.6 μm, width: 1.3 μm, pitch: 4 μm) consist of riblets, with different lengths ranging from 4 to 16 μm (Figure S1). Whereas Master 1 (Nickel mold) was provided by Sharklet Technologies, Master 2 (TiO_2-50) was made of a TiO_2-50 shark-skin-patterned sample. The soft PDMS molds were replicated from the masters and therefore contain the inverse structure of the master and can be used to imprint the original-tone pattern on PET substrates. Dispersions of NOA, TiO_2-10, TiO_2-50, and TiO_2–C were spin-coated onto PET substrates with sufficient residual solvent so that the coating had an appropriate viscosity (liquid enough) to fill the PDMS when placed in contact on top of the coating. The PDMS mold was kept on the substrate until the shark-skin microstructures were formed, which was about 30 min, although the pattern-transfer process was not optimized for cycle time. Other publications from our group show NIL patterning of titania surface patterns with cycle times of a few minutes or less.[32,36] NOA, TiO_2-10, and TiO_2-50 assemblies were cured under UV exposure, and ceramic

TiO_2–C shark-skin assemblies were cured under NIR irradiation. After completing the curing process, the PDMS mold was peeled off, revealing microstructured shark-skin-patterned films. The mechanism behind the pattern formation via solvent-assisted NIL is a result of the capillary force that drives the solution to form into the shape of the mold.[31,32] As the solvent evaporates through the air-permeable PDMS stamp, the patterned structures form.

Our goal was to fabricate all shark-skin-patterned surfaces with the same dimensions as those of the TiO_2–C shark-skin microstructures. Notably, as the solvent evaporates during imprinting, the TiO_2 NPs pack and shrink more than the polymer. Depending on the amount of solvent during imprinting, the dimensions of the features change, resulting in features with dimensions less than the mold dimensions, whereas polymer materials can be imprinted with a perfect replication of the master mold.[37] Thus, to make NOA and TiO_2-10 imprints with the same dimensions as those of TiO_2–C, we used a different master mold (Master 2) than the one used for TiO_2-50 and TiO_2–C shark-skin-patterned structures (Master 1).

The use of stable dispersions is a key requirement to obtain uniform filling of the stamp, which results in reproducible, well-replicated structures. Because of the high surface tension of aqueous solutions, wetting interactions between the solution and PDMS mold are not favorable without the use of surfactants. Organic solvents such as *N*-methyl-2-pyrrolidone (NMP) and methanol (MeOH) have a lower surface tension, which makes them preferable for solvent-assisted NIL. Moreover, the use of organic solvents and an elevated temperature (50 °C) increased solvent evaporation in solvent-assisted NIL, decreasing the overall imprint time. Thus, solvent exchange was conducted from water to a solvent mixture of NMP/MeOH, yielding a stable dispersion of 10–15 wt % TiO_2 NPs. MeOH, which is highly volatile, allows for fast film formation, whereas NMP, which is less volatile, evaporates more slowly and therefore allows sufficient time for the imprinting process. Furthermore, NMP is a common solvent to disperse both NOA and TiO_2 NPs. Relative humidity (RH) is also an important parameter to consider when trying to obtain reproducible patterned surfaces. At high RH (above 30%), spin-coated films become thinner.[32] Optimum humidity was determined to be below 20% RH. The spin-coating speed and time can be adjusted according to RH to obtain desirable thickness and fluidity of the film.

3.2. Characterization of the Composites

NOA is a UV-curable optical adhesive material that has been used as matrix for NP composites.[31,38] In our study, we chose NOA as a model nanoimprint lithography matrix for several reasons, including that NOA can homogeneously disperse TiO_2 NPs, NOA cures in several seconds to minutes depending on film thickness and light intensity, and NOA has favorable mechanical properties, such as high modulus.[31,39] TiO_2-10 and TiO_2-50 shark-skin microstructures were prepared as 10 and 50 wt % TiO_2 loading to NOA. The loading of TiO_2 NPs in samples TiO_2-10 and TiO_2-50 was measured by TGA and confirmed to be 10 and 50 wt %, respectively (Figure S2).

Fully ceramic TiO_2–C samples were prepared using a 90 wt % TiO_2 and 10 wt % TEOS dispersion, in which TEOS polymerizes under NIR irradiation to create a SiO_2 binder to obtain ceramic coatings. The resulting cross-linked silica structures generated upon heating

prevent deformation of microstructures after immersing the films in an aqueous solution. The samples without NIR curing were not stable in water overnight. Light sintering has several advantages compared with thermal sintering such as rapid process times and ability to sintering directly on flexible polymeric substrates. In previous works, NIR heating of TiO_2 NPs was performed on metallic and fluorine-doped tin oxide glass substrates. NIR light was absorbed by the substrates and heated the film up to 700 °C in 12.5 s.[40,41] The PET substrate does not absorb NIR; however, because of the absorption of TiO_2 above 1800 nm,[42] heat radiation makes silica binding form quickly (10 s). Through NIR light annealing, ceramic TiO_2–C shark-skin structures were obtained on flexible PET substrates.

TEM images of TiO_2 NPs and TiO_2-10, TiO_2-50, and TiO_2–C films are shown in Figure S3. The average TiO_2 NP size was calculated to be 8.7 ± 4.5 nm by measuring at least 100 particles across multiple TEM images. The TEM micrographs indicate that the TiO_2-10 composites exhibit a homogeneous dispersion of NPs, without any agglomeration; this is in contrast with what was observed for the TiO_2-50 composite. In the ceramic sample, TiO_2–C, a high concentration of nanoparticles was observed, and as expected, the quick NIR treatment did not change the average size of the NPs.

The mechanical properties of composites were characterized using nanoindentation.[43,44] During the measurements, indentation depth did not exceed 10% of the film thickness to prevent substrate effects. Hardness and reduced modulus values are shown in Table 1. The hardness values of NOA and TiO_2-10 were determined to be 279 ± 14 and 278 ± 32 MPa, respectively. There was not a significant difference in the hardness and modulus values between NOA and TiO_2-10. However, as the loading of TiO_2 NPs increased, from TiO_2-10 to TiO_2-50, the hardness decreased significantly from 278 ± 32 to 204 ± 81 MPa and the modulus decreased from 4.6 ± 0.4 to 4.0 ± 0.8 GPa, potentially due to a decreased cross-linking density of the NOA matrix. Under UV exposure, the TiO_2 present in the composite materials may be preventing full curing due to the UV absorption of TiO_2. The hardness and modulus of the fully ceramic TiO_2–C films were determined to be 490 ± 68 MPa and 16 ± 2 GPa, respectively, which were significantly higher than those of the polymeric composite materials. As expected, the fully ceramic nature of these films gave rise to ~75 and ~233% increase in hardness and reduced modulus, respectively, compared to those of the polymeric composite materials.

3.3. Characterization of Shark-Skin-Patterned Surfaces

The SEM micrographs of shark-skin-patterned surfaces in NOA (Figure 1a), TiO_2-10 (Figure 1b), TiO_2-50 (Figure 1c,d), and TiO_2–C (Figure 1e,f) are shown in Figure 1. The dimensions of the shark-skin imprints were determined using an optical profilometer and from SEM imaging. The height, width, and spacing of riblets were ~1.6, 1.3, and 2.7 μm, respectively (Figure 1). All of the features were replicated uniformly in size and shape over a large area (4 cm × 4 cm). Digital pictures of the shark-skin patterns on PET substrates are shown in Figure S4. We have also prepared NOA* (100% NOA) shark skin with the same dimensions as those of Master 1 as a control patterned surface, Figure S5. The antifouling properties of NOA* (height: 3 μm, width: 2 μm, spacing: 2 μm) patterned surfaces were compared with those of NOA (height: 1.6 μm, width: 1.3 μm, spacing: 2.7 μm) patterned

surfaces to understand if increasing the spacing between the features would affect the adhesion of *E. coli*.

After imprints were successfully achieved, their advancing, receding, and static water contact angles were determined, and the results are shown in Figure 2. As the concentration of TiO_2 NPs in the patterned surfaces increased, the static contact angle decreased from 139 to 106°. This is due to the high affinity of TiO_2 for water. The contact angles were recorded parallel and perpendicular to features due to anisotropy of the surfaces. Difference in contact angles from different directions is expected and can be explained by the energy barrier, which was observed for discontinuous gradient surfaces, consistent with Sharklet AF surfaces.[45] In addition, a higher contact angle hysteresis (CAH) was observed for the photocatalytic shark-skin microstructures (~100°) compared to that for the NOA shark-skin surface (~30°). This can be explained by chemical heterogeneous composition and the interaction between TiO_2 NPs and water.[46,47] Despite the high CAH observed in the photocatalytic shark-skin surfaces, these surfaces demonstrated a great ability to resisting the initial attachment of bacteria. Overall, the antifouling property of shark-skin-patterned surfaces is closely linked to the organisms' size relative to the surface topography and potentially also due to biological mechanisms. The CAH of a surface does not play the key role in repelling microbes from patterned surfaces.[15,48–50]

3.4. Antifouling Activity of Shark-Skin-Patterned Surfaces

The 24 h antifouling properties of shark-skin-patterned surfaces were tested using the model Gram-negative microorganism, *E. coli*, and compared to those of smooth chemistry controls (Figures 3 and S6). Bacterial adhesion is influenced by many factors, including the topography, chemistry, and mechanical properties of a surface.[34,51,52] Shark-skin-patterned surfaces (of all composite chemistries) reduced bacterial surface area coverage to less than 1% of the total surface area of the sample. NOA, TiO_2-10, TiO_2-50, and TiO_2–C shark-skin-patterned surfaces displayed surface area coverages of 0.67 ± 0.20, 0.57 ± 0.18, 0.58 ± 0.17, and 0.79 ± 0.22%, respectively. Compared with smooth films with the same chemistry, shark-skin-patterned NOA surfaces reduced bacterial area coverage by up to 85%, and TiO_2-10, TiO_2-50, and TiO_2–C surfaces reduced bacterial area coverage by up to 70%. Compared with flat PET controls, shark-skin-patterned surfaces reduced *E. coli* attachment by up to 80% (Figure S6).

Although smooth TiO_2 composites decreased the bacterial attachment up to 60% compared with NOA smooth samples, there was no significant difference between the antifouling activity of the NOA, TiO_2-10, TiO_2-50, and TiO_2–C shark- skin-patterned surfaces. These results indicate that surface topography dominated the chemical composition of the shark-skin surfaces in terms of reducing bacterial adhesion. Moreover, doubling the height and increasing the aspect ratio and spacing of the features, NOA* (height: 3 μm, aspect ratio: 1.5, spacing: 2 μm) did not elicit a statistically significant difference in *E. coli* area coverage compared with NOA (height: 1.6 μm, aspect ratio: 1.2, spacing: 2.7 μm) shark-skin surfaces (Figure S6). Although Schumacher et al. found that increasing the aspect ratio of PDMS Sharklet AF surfaces significantly reduced the attachment of *Ulva* spores and barnacle cyprids by up to 42–45%, this was due to the larger size of their organism.[53]

The *E. coli* that adhered to the surfaces was observed among the features (Figure S7), consistent with previous studies.[23] If the spacing among the features is larger than the width of the bacteria, bacteria fall between the patterns and attach to the spaces rather than being repelled by the features.[15,54,55] However, because of the physical disturbance of the microstructures, cell-to-cell interactions decrease and delay colony formation. In the long term, the bacteria can still form a biofilm if the adhered bacteria continue to live on the engineered surfaces; thus, a killing mechanism is needed to inactivate the settled microbes.

3.5. Antibacterial Activity of TiO_2 NP Composites

The photocatalytic antibacterial activity of flat films was evaluated using the model microbial species *E. coli* and *S. aureus* (Figure 4). All composite compositions that contained TiO_2 NPs (TiO_2-10, TiO_2-50, and TiO_2–C) showed a significant antibacterial activity, 90 ± 4, 83 ± 6, and 93 ± 2%, respectively, for *E. coli*, and 83 ± 5, 80 ± 8, and 80 ± 7%, respectively, for *S. aureus* after 1 h of UV light exposure. The control samples, flat PET and NOA, showed only baseline inactivation, ~5% killing. Notably, there was not a significant difference in the killing efficiency between the lowest, TiO_2-10, and the highest, TiO_2–C, TiO_2 concentration samples. The concentration, size, and phase of TiO_2, the polymer matrix, and additives are the main factors that influence the antibacterial activity of TiO_2 NPs.[26,56,57] In our experiments, we used anatase phase TiO_2 NPs, which were reported to exhibit a higher photocatalytic activity compared to that of rutile-phase NPs.[26,58]

Another important factor is how homogeneous the dispersion of NPs is within the matrix. Kubacka et al. reported that by using only 2 wt % TiO_2 NPs (~9 nm) in ethylene–vinyl alcohol copolymer composite, they had a 6.3 log reduction of *P. aeruginosa* after 30 min because of well-distributed NPs.[59] A homogeneous dispersion of nanoparticles increases the available surface area and diffusion of reactive hydroxyl radicals and superoxide ions and therefore increases their photocatalytic activity. Here, composites were prepared without using any ligands or dispersing agents and still resulted in a sufficiently homogeneous dispersion using a straightforward solution processing technique. Alternatively, one could also incorporate metal NPs such as copper or silver into the TiO_2 composite material. In this way, the band gap decreases and the absorption of light shifts toward the visible light.[60,61] Other factors that influence the antibacterial performance are the UV source and the source intensity.[57] Here, we used a UV lamp (365 nm) with a weak light intensity of 1.0 mW/cm^2, which still had an excellent antibacterial activity in 1 h. Notably, whereas TiO_2 is known to have degradative effects on organic materials, with low-enough UV intensity, polymer composites can maintain their performance. While the degradation kinetics of polymer composites was not investigated because it was beyond the scope of this project, we hypothesize that because the UV exposure was sufficiently low, minimal degradation occurred.

4. CONCLUSIONS

We have presented a simple strategy to fabricate multifunc-tional shark-skin surfaces with antifouling and antibacterial properties. Moreover, ceramic shark-skin coatings (TiO_2–C) were successfully imprinted on a flexible PET substrate and cured using only 10 s of NIR

irradiation. We studied the wetting and mechanical properties of shark-skin-patterned surfaces as a function of TiO_2 loading in the composites. The introduction of TiO_2 NPs increased CAH from 30 to 100° on shark-skin surfaces. The hardness and reduced modulus were not significantly altered by increasing TiO_2 NPs up to 50 wt %; however, the hardness of the ceramic TiO_2–C sample increased by up to 2 times compared to that of NOA, TiO_2-10, and TiO_2-50. Shark-skin surfaces reduced the attachment of *E. coli* by 70–85% and killed 85–95% of *E. coli* and *S. aureus* after 1 h of UV light exposure. To the best of our knowledge, this work represents the first reported use of antibacterial NPs in shark-skin patterns. The combination of passive and active strategies on a single surface is the most promising material design strategy to control bacterial fouling. Our fabrication technique is a roll-to-roll compatible method that can be scaled up to be used for practical applications.

Supplementary Material

Refer to Web version on PubMed Central for supplementary material.

Acknowledgments

This research was kindly supported by U.S. Army Laboratories (ARL W911NF-15-0024 and W911NF-15-2-0026). We also thank Sharklet Technologies for providing the Sharklet AF master mold and Carpe Diem Technologies for providing a UV meter. K.W.K. was supported by the National Research Service Award T32 GM008515 from the National Institutes of Health. I.S.K. acknowledges the support of the National Science Foundation NRT program (DGE-1545399). F.D.A. acknowledges R. Kothari, J. John, C. Li, and Y. Li for their help with experimental procedures.

References

1. Boyce JM, Havill NL, Otter JA, Adams NMT. Widespread Environmental Contamination Associated With Patients With Diarrhea and Methicillin-Resistant *Staphylococcus aureus* Colonization of the Gastrointestinal Tract. Infect Control Hosp Epidemiol. 2007; 28:1142–1147. [PubMed: 17828690]
2. Carling PC, Briggs J, Hylander D, Perkins J. An Evaluation of Patient Area Cleaning in 3 Hospitals Using a Novel Targeting Methodology. Am J Infect Control. 2006; 34:513–519. [PubMed: 17015157]
3. Weber DJ, Rutala WA, Miller MB, Huslage K, Sickbert-Bennett E. Role of Hospital Surfaces in the Transmission of Emerging Health Care-Associated Pathogens: Norovirus, Clostridium Difficile, and Acinetobacter Species. Am J Infect Control. 2010; 38:S25–S33. [PubMed: 20569853]
4. Pogorzelska-Maziarz M, Carter EJ, Manning ML, Larson EL. State Health Department Requirements for Reporting of Antibiotic-Resistant Infections by Providers, United States, 2013 and 2015. Public Health Rep. 2017; 132:32–36. [PubMed: 28005484]
5. Centers for Disease Control and Prevention (CDC). Antibiotic Resistance Threats in the United States, 2013. U.S. Department of Health and Human Services, CDC; Atlanta, Georgia: 2013. http://www.cdc.gov/drugresistance/threat-report-2013
6. Stewart PS, Costerton JW. Antibiotic Resistance of Bacteria in Biofilms. Lancet. 2001; 358:135–138. [PubMed: 11463434]
7. Costerton JW, Stewart PS, Greenberg EP. Bacterial Biofilms: A Common Cause of Persistent Infections. Science. 1999; 284:1318–1322. [PubMed: 10334980]
8. Lu Y, Yue Z, Wang W, Cao Z. Strategies on Designing Multifunctional Surfaces to Prevent Biofilm Formation. Front Chem Sci Eng. 2015; 9:324–335.
9. Zhao N, Wang Z, Cai C, Shen H, Liang F, Wang D, Wang C, Zhu T, Guo J, Wang Y, Liu X, Duan C, Wang H, Mao Y, Jia X, Dong H, Zhang X, Xu J. Bioinspired Materials: From Low to High Dimensional Structure. Adv Mater. 2014; 26:6994–7017. [PubMed: 25212698]

10. Bhushan B. Biomimetics: Lessons from Nature-An Overview. Philos Trans R Soc, A. 2009; 367:1445–1486.
11. Liu K, Jiang L. Bio-Inspired Self-Cleaning Surfaces. Annu Rev Mater Res. 2012; 42:231–263.
12. Scardino AJ, de Nys R. Mini Review: Biomimetic Models and Bioinspired Surfaces for Fouling Control. Biofouling. 2011; 27:73–86. [PubMed: 21132577]
13. Hasan J, Chatterjee K. Recent Advances in Engineering Topography Mediated Antibacterial Surfaces. Nanoscale. 2015; 7:15568–15575. [PubMed: 26372264]
14. Genzer J, Efimenko K. Recent Developments in Super-hydrophobic Surfaces and Their Relevance to Marine Fouling: A Review. Biofouling. 2006; 22:339–360. [PubMed: 17110357]
15. Graham M, Cady N. Nano and Microscale Topographies for the Prevention of Bacterial Surface Fouling. Coatings. 2014; 4:37–59.
16. Liu K, Jiang L. Bio-Inspired Self-Cleaning Surfaces. Annu Rev Mater Res. 2012; 42:231–263.
17. Bechert DW, Bruse M, Hage W. Experiments with Three-Dimensional Riblets as an Idealized Model of Shark Skin. Exp Fluids. 2000; 28:403–412.
18. Bixler GD, Bhushan B. Fluid Drag Reduction with Shark-Skin Riblet Inspired Microstructured Surfaces. Adv Funct Mater. 2013; 23:4507–4528.
19. Carman ML, Estes TG, Feinberg AW, Schumacher JF, Wilkerson W, Wilson LH, Callow ME, Callow JA, Brennan AB. Engineered Antifouling Microtopographies–Correlating Wettability with Cell Attachment. Biofouling. 2006; 22:11–21. [PubMed: 16551557]
20. Schumacher JF, Carman ML, Estes TG, Feinberg AW, Wilson LH, Callow ME, Callow JA, Finlay JA, Brennan AB. Engineered Antifouling Microtopographies-Effect of Feature Size, Geometry, and Roughness on Settlement of Zoospores of the Green Alga. Ulva Biofouling. 2007; 23:55–62. [PubMed: 17453729]
21. Chung KK, Schumacher JF, Sampson EM, Burne RA, Antonelli PJ, Brennan AB. Impact of Engineered Surface Microtopography on Biofilm Formation of *Staphylococcus aureus*. Biointerphases. 2007; 2:89–94. [PubMed: 20408641]
22. Schumacher JF, Long CJ, Callow ME, Finlay JA, Callow JA, Brennan AB. Engineered Nanoforce Gradients for Inhibition of Settlement (Attachment) of Swimming Algal Spores. Langmuir. 2008; 24:4931–4937. [PubMed: 18361532]
23. Reddy ST, Chung KK, McDaniel CJ, Darouiche RO, Landman J, Brennan AB. Micropatterned Surfaces for Reducing the Risk of Catheter-Associated Urinary Tract Infection: An *In Vitro* Study on the Effect of Sharklet Micropatterned Surfaces to Inhibit Bacterial Colonization and Migration of Uropathogenic *Escherichia coli*. J Endourol. 2011; 25:1547–1552. [PubMed: 21819223]
24. Li Y, Zhang W, Niu J, Chen Y. Mechanism of Photogenerated Reactive Oxygen Species and Correlation with the Antibacterial Properties of Engineered Metal-Oxide Nanoparticles. ACS Nano. 2012; 6:5164–5173. [PubMed: 22587225]
25. Kubacka A, Diez MS, Rojo D, Bargiela R, Ciordia S, Zapico I, Albar JP, Barbas C, Martins dos Santos VAP, Fernandez-Garcia M, Ferrer M. Understanding the Antimicrobial Mechanism of TiO_2-Based Nanocomposite Films in a Pathogenic Bacterium. Sci Rep. 2014; 4:4134. [PubMed: 24549289]
26. Fu G, Vary PS, Lin C-T. Anatase TiO_2 Nanocomposites for Antimicrobial Coatings. J Phys Chem B. 2005; 109:8889–8898. [PubMed: 16852057]
27. Kühn KP, Chaberny IF, Massholder K, Stickler M, Benz VW, Sonntag HG, Erdinger L. Disinfection of Surfaces by Photocatalytic Oxidation with Titanium Dioxide and UVA Light. Chemosphere. 2003; 53:71–77. [PubMed: 12892668]
28. Carp O, Huisman CL, Reller A. Photoinduced Reactivity of Titanium Dioxide. Prog Solid State Chem. 2004; 32:33–177.
29. Hashimoto K, Irie H, Fujishima A. TiO_2 Photocatalysis: A Historical Overview and Future Prospects. Jpn J Appl Phys. 2005; 44:8269–8285.
30. Fujishima A, Rao TN, Tryk DA. Titanium Dioxide Photocatalysis. J Photochem Photobiol, C. 2000; 1:1–21.
31. Beaulieu MR, Hendricks NR, Watkins JJ. Large-Area Printing of Optical Gratings and 3D Photonic Crystals Using Solution-Processable Nanoparticle/Polymer Composites. ACS Photonics. 2014; 1:799–805.

32. Kothari R, Beaulieu MR, Hendricks NR, Li S, Watkins JJ. Direct Patterning of Robust 1-D, 2-D and 3-D Crystalline Metal Oxide Nanostructures Using Imprint Lithography and Nanoparticle Dispersion Inks. Chem Mater. 2017; 29:3908–3918.
33. Moran IW, Briseno AL, Loser S, Carter KR. Device Fabrication by Easy Soft Imprint Nano-Lithography. Chem Mater. 2008; 20:4595–4601.
34. Kolewe KW, Peyton SR, Schiffman JD. Fewer Bacteria Adhere to Softer Hydrogels. ACS Appl Mater Interfaces. 2015; 7:19562–19569. [PubMed: 26291308]
35. Rieger KA, Cho HJ, Yeung HF, Fan W, Schiffman JD. Antimicrobial Activity of Silver Ions Released from Zeolites Immobilized on Cellulose Nano Fiber Mats. ACS Appl Mater Interfaces. 2016; 8:3032–3040. [PubMed: 26788882]
36. Li W, Zhou Y, Howell IR, Gai Y, Naik AR, Li S, Carter KR, Watkins JJ. Direct Imprinting of Scalable, High-Performance Woodpile Electrodes for Three-Dimensional Lithium-Ion Nanobatteries. ACS Appl Mater Interfaces. 2018; 10:5447–5454. [PubMed: 29369613]
37. Guo LJ. Nanoimprint Lithography: Methods and Material Requirements. Adv Mater. 2007; 19:495–513.
38. Li C, Colella NS, Watkins JJ. Low-Temperature Fabrication of Mesoporous Titanium Dioxide Thin Films with Tunable Refractive Indices for One-Dimensional Photonic Crystals and Sensors on Rigid and Flexible Substrates. ACS Appl Mater Interfaces. 2015; 7:13180–13188. [PubMed: 26023903]
39. Chen X, Sun J, Shen J. Patterning of Layer-by-Layer Assembled Organic-Inorganic Hybrid Films: Imprinting versus Lift-Off. Langmuir. 2009; 25:3316–3320. [PubMed: 19437792]
40. Watson T, Mabbett I, Hongxia W, Peter L, Worsley D. Ultrafast near Infrared Sintering of TiO_2 Layers on Metal Substrates for Dye-Sensitized Solar Cells. Prog Photovoltaics. 2011; 19:482–486.
41. Hooper K, Carnie M, Charbonneau C, Watson T. Near Infrared Radiation as a Rapid Heating Technique for TiO_2 Films on Glass Mounted Dye-Sensitized Solar Cells. Int J Photoenergy. 2014; 2014:1–8.
42. Jeevanandam P, Mulukutla RS, Phillips M, Chaudhuri S, Erickson LE, Klabunde KJ. Near Infrared Reflectance Properties of Metal Oxide Nanoparticles. J Phys Chem C. 2007; 111:1912–1918.
43. Oliver WC, Pharr M. An Improved Technique for Determining Hardness and Elastic Modulus Using Load and Displacement Sensing Indentation Experiments. J Mater Res. 1992; 7:1564–1583.
44. Oliver WC, Pharr GM. Measurement of Hardness and Elastic Modulus by Instrumented Indentation: Advances in Understanding and Refinements to Methodology. J Mater Res. 2004; 19:3–20.
45. Long CJ, Schumacher JF, Brennan AB. Potential for Tunable Static and Dynamic Contact Angle Anisotropy on Gradient Microscale Patterned Topographies. Langmuir. 2009; 25:12982–12989. [PubMed: 19603771]
46. Gao L, McCarthy TJ. Contact Angle Hysteresis Explained. Langmuir. 2006; 22:6234–6237. [PubMed: 16800680]
47. Youngblood JP, McCarthy TJ. Ultrahydrophobic Polymer Surfaces Prepared by Simultaneous Ablation of Polypropylene and Sputtering of Poly(tetrafluoroethylene) Using Radio Frequency Plasma. Macromolecules. 1999; 32:6800–6806.
48. Ucar IO, Cansoy CE, Erbil HY, Pettitt ME, Callow ME, Callow JA. Effect of Contact Angle Hysteresis on the Removal of the Sporelings of the Green Alga *Ulva* from the Fouling-Release Coatings Synthesized from Polyolefin Polymers. Biointerphases. 2010; 5:75–84. [PubMed: 21171721]
49. Alexander MR, Williams P. Water Contact Angle Is Not a Good Predictor of Biological Responses to Materials. Biointerphases. 2017; 12:02C201.
50. Dobosz KM, Kolewe KW, Schiffman JD. Green Materials Science and Engineering Reduces Biofouling: Approaches for Medical and Membrane-Based Technologies. Front Microbiol. 2015; 6:196. [PubMed: 25852659]
51. Song F, Koo H, Ren D. Effects of Material Properties on Bacterial Adhesion and Biofilm Formation. J Dent Res. 2015; 94:1027–1034. [PubMed: 26001706]

52. Anselme K, Davidson P, Popa AM, Giazzon M, Liley M, Ploux L. The Interaction of Cells and Bacteria with Surfaces Structured at the Nanometre Scale. Acta Biomater. 2010; 6:3824–3846. [PubMed: 20371386]

53. Schumacher JF, Aldred N, Callow ME, Finlay JA, Callow JA, Clare AS, Brennan AB. Species-Specific Engineered Antifouling Topographies: Correlations between the Settlement of Algal Zoospores and Barnacle Cyprids. Biofouling. 2007; 23:307–317. [PubMed: 17852066]

54. Perni S, Prokopovich P. Micropatterning with Conical Features Can Control Bacterial Adhesion on Silicone. Soft Matter. 2013; 9:1844–1851.

55. Whitehead KA, Colligon J, Verran J. Retention of Microbial Cells in Substratum Surface Features of Micrometer and Sub-Micrometer Dimensions. Colloids Surf, B. 2005; 41:129–138.

56. Fujishima A, Zhang X, Tryk DA. TiO_2 Photocatalysis and Related Surface Phenomena. Surf Sci Rep. 2008; 63:515–582.

57. Benabbou AK, Derriche Z, Felix C, Lejeune P, Guillard C. Photocatalytic Inactivation of *Escherischia Coli*. Effect of Concentration of TiO_2 and Microorganism, Nature, and Intensity of UV Irradiation. Appl Catal, B. 2007; 76:257–263.

58. Matsunaga T, Tomoda R, Nakajima T, Wake H. Photoelectrochemical Sterilization of Microbial Cells by Semiconductor Powders. FEMS Microbiol Lett. 1985; 29:211–214.

59. Kubacka A, Serrano C, Ferrer M, Lunsdorf H, Bielecki P, Cerrada ML, Fernandez-García M, Fernandez-García M. High- Performance Dual-Action Polymer-TiO_2 Nanocomposite Films via Melting Processing. Nano Lett. 2007; 7:2529–2534. [PubMed: 17625905]

60. Leyland NS, Podporska-Carroll J, Browne J, Hinder SJ, Quilty B, Pillai SC. Highly Efficient F, Cu Doped TiO_2 Anti- Bacterial Visible Light Active Photocatalytic Coatings to Combat Hospital-Acquired Infections. Sci Rep. 2016; 6:24770. [PubMed: 27098010]

61. Page K, Wilson M, Parkin IP. Antimicrobial Surfaces and Their Potential in Reducing the Role of the Inanimate Environment in the Incidence of Hospital-Acquired Infections. J Mater Chem. 2009; 19:3819–3831.

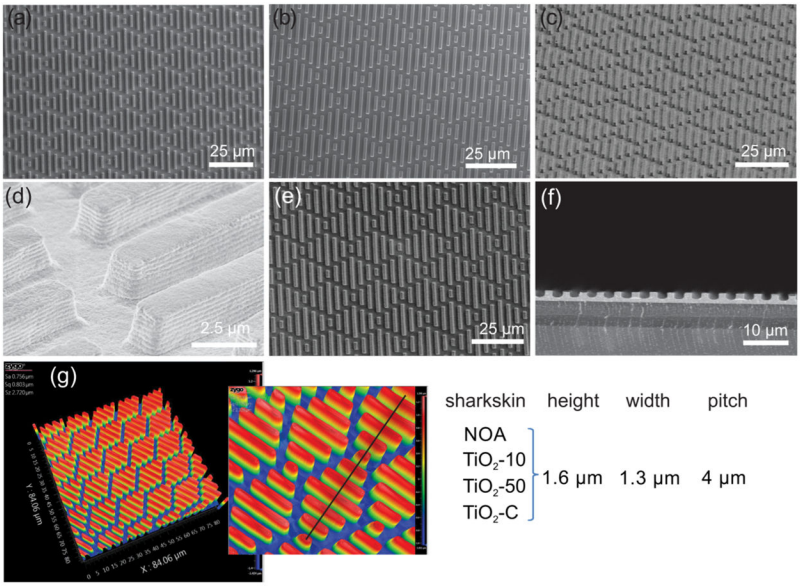

Figure 1.

SEM images and dimensions of shark-skin patterns with different composites. (a) NOA (top view), (b) TiO_2-10 (top view), (c) TiO_2-50 (45° tilted), (d) TiO_2-50 (45° tilted, high mag.), (e) TiO_2–C (top view), (f) TiO_2–C (cross section), and (g) optical profilometry images and dimensions of shark-skin-patterned surfaces.

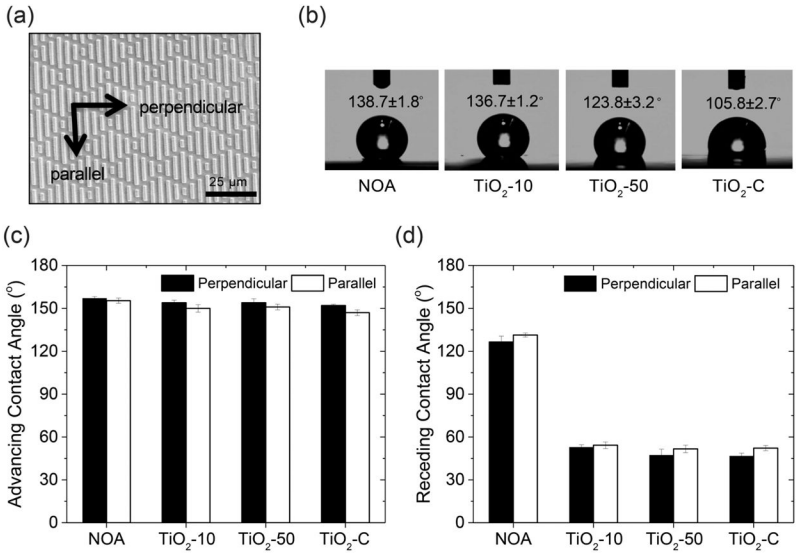

Figure 2.

Water contact angle analysis of shark-skin-patterned surfaces. (a) Schematic representation of perpendicular and parallel directions to the shark-skin patterns. (b) Static water contact angle on shark-skin-patterned surfaces. (c) Advancing water contact angle perpendicular and parallel to the shark-skin-patterned surfaces. (d) Receding water contact angle perpendicular and parallel to the shark-skin-patterned surfaces. Error bars denote standard deviation.

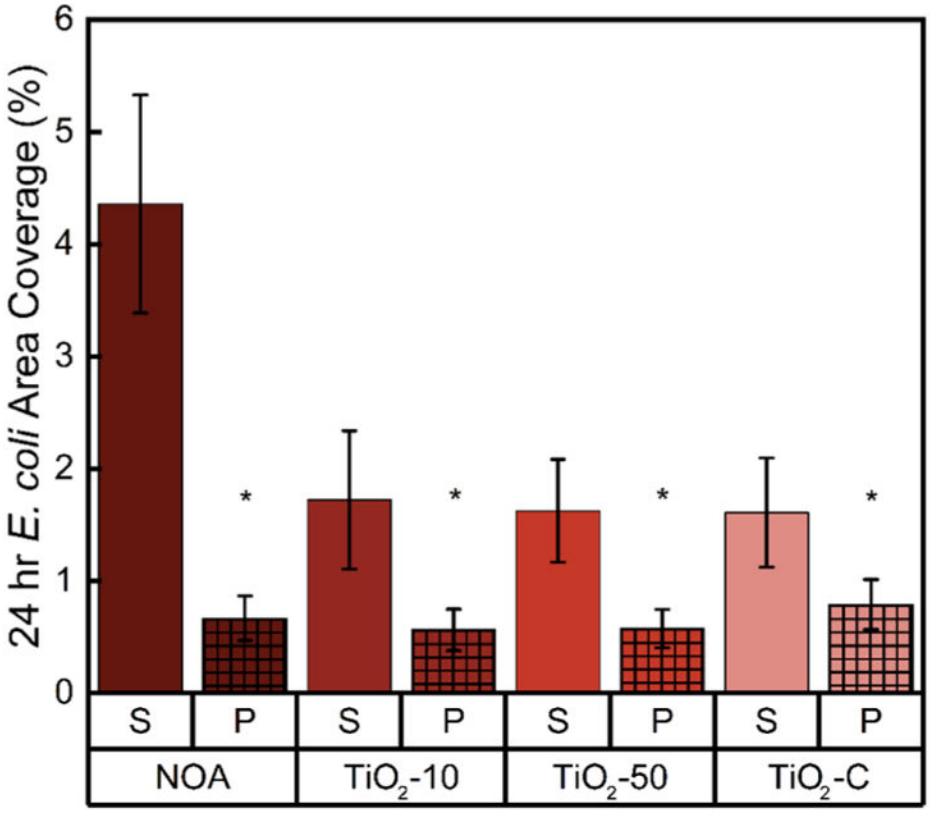

Figure 3.

24 h area coverage of surface-adhered *E. coli* on smooth films (S) versus patterned surfaces (P) of NOA, TiO_2-10, TiO_2-50, and TiO_2–C. An asterisk (*) denotes 95% significance between smooth and patterned samples. Error bars denote standard error.

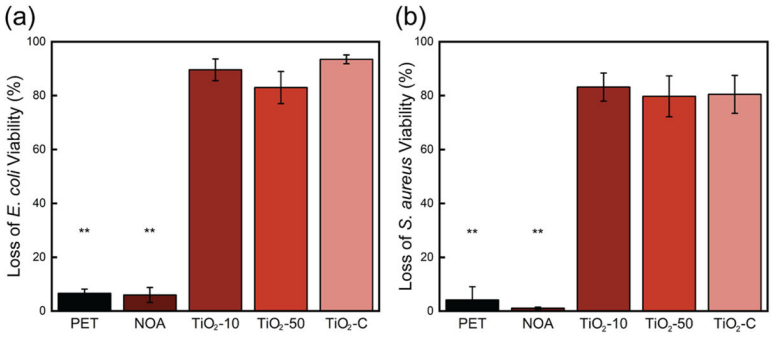

Figure 4.

Loss of (a) *E. coli* and (b) *S. aureus* viability after 1 h of UV exposure to planar TiO_2-10, TiO_2-50, and TiO_2–C films. Control PET and NOA surfaces (no TiO_2) are also shown. Two asterisks (**) denote 99% significance between control and TiO_2-containing samples. Error bars denote standard error.

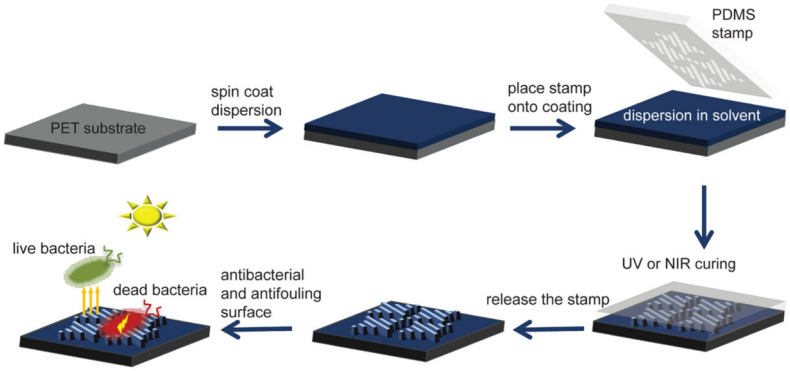

Scheme 1.

Schematic Representation of the Fabrication Process of Shark-Skin Patterns Using a PDMS Soft Stamp on Flexible PET Substrates

Author Manuscript

Author Manuscript

Author Manuscript

Table 1

Nanomechanical Analysis of Composite Materials*

	NOA	TiO_2-10	TiO_2-50	TiO_2–C
hardness (MPa)	$279^a \pm 14$	$278^a \pm 32$	$204^b \pm 81$	$490^c \pm 68$
reduced modulus (GPa)	$4.8^a \pm 0.2$	$4.6^a \pm 0.4$	$4.0^a \pm 0.8$	$16^b \pm 2$

*Superscript letters (a,b) within a row indicate statistically significant differences at $p < 0.05$ level (Tukey's honest significant difference). Standard deviation is displayed.